Carbon 155 (2019) 697–705

Contents lists available at ScienceDirect

Carbon

journal homepage: www.elsevier.com/locate/carbon

# Tuning graphene mechanical anisotropy via defect engineering

Bowen Zheng, Grace X. Gu*

*Department of Mechanical Engineering, University of California, Berkeley, CA, 94720, USA*

ARTICLE INFO

*Article history:*
Received 27 June 2019
Received in revised form
21 August 2019
Accepted 2 September 2019
Available online 3 September 2019

ABSTRACT

Exceptional mechanical properties of graphene have been extensively studied and leveraged in applications of a broad variety. The fine-tuning of the degree of graphene mechanical anisotropy, however, remains not well understood today. In this paper, a defect engineering strategy is adopted to tune the anisotropic property of monolayer graphene. Mechanical properties of various defect designs, from defect designs consisting of basic elements to more complex patterned graphene kirigami, are systematically discussed and numerically studied using molecular dynamics simulations. A novel stress-ratio-versus-strain-ratio graph is proposed to visualize and rationalize the tuning of mechanical anisotropy of defected graphene sheet. Through our defect designs, all the four quadrants of the 2D ratio graph are covered, indicating a high capability and versatility of fine-tuning the mechanical properties of graphene in different directions. This research, which investigates the tunability of graphene mechanical anisotropy via defect design, sheds light on the new possibility of fine-tuning mechanical properties of other 2D materials and has the potential to improve materials for applications such as stretchable electronics and supercapacitor devices.



## 1. Introduction

Graphene, a 2D material consisting of hexagonally packed carbon atoms, has been exhibiting remarkable capabilities in a broad range of state-of-the-art research fields due to its superlative electronic [1–3], thermal [4,5], and mechanical [6,7] properties since its discovery [8]. Despite being one-atom thick, the monolayer graphene possesses an exceptional combination of mechanical properties, including an ultrahigh Young's modulus of ~1 TPa [6] and an extreme tensile strength of 130 GPa [6]. These mechanical properties make graphene not only ideal for the fabrication of ultra-strong fibers [9,10] and membranes [11,12], but also an elite candidate for emerging technologies such as stretchable electronics [13,14], micro-/nano-electromechanical systems (M-/N-EMS) [15–17], and supercapacitor devices [18–20], among others. In addition, these properties of graphene can be tuned by means of chemical doping [21,22] and functionalization [23], making graphene a favorable material choice for a variety of research purposes.

Another notable mechanical property of monolayer graphene is its chirality-related mechanical anisotropy - the mechanical properties in one direction differ intrinsically from those in another direction [24]. Ni et al. observed the anisotropic mechanical properties using molecular dynamics (MD) simulation and studied fracture modes and stiffness property in different directions [24]. Fan et al. studied anisotropic mechanical properties of monolayer graphene using density functional theory (DFT) method and related the intrinsic anisotropy to the $sp^2$ hybridization of the hexagonal lattice [25]. Pereira et al. studied the anisotropic thermal and mechanical properties of phagraphene, a newly theoretically proposed defective graphene structure consisting of pentagonal, heptagonal and hexagonal rings [26]. Although substantial research endeavors have been poured into the anisotropic nature of graphene, a systematic fine-tuning paradigm of graphene mechanical anisotropy remains not well understood and unexplored to date. Hence, a systematic investigation on graphene mechanical anisotropy contributes to the literature by providing insight into designing graphene with tunable properties which can potentially circumvent property tradeoffs such as between strength and ductility. Also, from the perspective of engineering applications, the tunability of graphene anisotropy has the potential to improve the mechanical integrity of biological composites and flexible electronics by directing crack propagation and energy dissipation to more ductile materials [27].

Graphene kirigami [28], a defect engineering strategy of graphene inspired by the art of paper cutting, has shown great potential in tuning the mechanical [28,29] and thermal [30]

* Corresponding author.
*E-mail address:* ggu@berkeley.edu (G.X. Gu).

https://doi.org/10.1016/j.carbon.2019.09.008
0008-6223/

properties of graphene. While one research direction in tuning properties of graphene involves adding a second material to make a nanocomposite [31–33], graphene kirigami research can offer property tunability with just cuts. Similar design concept such as graphene nanomesh [34–36] has also shown to be successful. Because of the high design freedom of defect engineering [37], it is possible and rational to design particular defect pattern to realize the specific requirement of anisotropic property, or to produce a counterintuitive isotropic graphene.

In this study, we explore the potential of fine-tuning the mechanical anisotropy of monolayer graphene via defect design, from defect designs consisting of basic elements to more complex patterned graphene kirigami. For basic defect designs, the influences of defect length, obliquity, offset from the center, and number of parallel defects are separately discussed. For more complex defect designs, network-like graphene kirigami and graphene kirigami with parallel interior and exterior cuts are investigated. MD simulations are conducted to study the mechanical properties of these proposed defected graphene designs. A novel stress-ratio-versus-strain-ratio graph is proposed to visualize and rationalize the tuning of mechanical anisotropy of defected graphene sheets. Through our defect design, all the four quadrants of the 2D ratio graph are covered, indicating a high capability and versatility of fine-tuning the mechanical properties of graphene in both directions. More complex designs such as designs involving curved defects as well as other 2D materials will be covered in future work.

The paper is developed as follows. Section 2 provides the necessary information of simulated monolayer graphene and MD simulation setup, together with the benchmark results of pristine graphene. Section 3 presents the results of graphene with a variety of designs consisting of basic defect elements. Section 4 provides a deeper dive into graphene with more complex defect designs to pursue more advanced tuning capability. Section 5 provides concluding remarks and possible areas of future directions.

## 2. System description and MD simulation setup

To explore the potential of fine-tuning anisotropic properties using defect engineering, square-shaped monolayer graphene is chosen to study in order to draw a fair comparison between the mechanical properties in the zigzag and armchair directions. A schematic of simulated graphene and loading conditions is provided in Fig. 1(a), where the graphene edge lengths in zigzag and armchair directions are $L_Z = 110.3$ Å and $L_A = 112.0$ Å, respectively, consisting of 4966 atoms at the maximum (graphene sheets with defects to be covered in the following sections contain less atoms). The length of the covalent C–C bond in the initial configuration is 1.421 Å and after equilibrium the average bond length is calculated to be 1.399 Å. Tensile loading is applied uniformly on one side of the graphene with the opposite side fixed.

To investigate the mechanical properties of monolayer graphene with designed defects, in this study, MD simulations are performed using the open-source code LAMMPS (Large-scale Atomic/Molecular Massively Parallel Simulator) [38]. The interactions of carbon atoms are simulated with Adaptive Intermolecular Reactive Empirical Bond Order (AIREBO) potential, which is capable to accurately model the bond breaking and reforming [39,40] involved in the fracture and failure processes. The AIREBO potential consists of a REBO term to model short-ranged interaction, and a Lennard-Jones (LJ) term to model long-ranged interaction, as can be formulated as

$$E = \frac{1}{2}\sum_i \sum_{j \neq i} \left( E_{ij}^{\mathrm{REBO}} + E_{ij}^{\mathrm{LJ}} \right) \tag{1}$$

where $E$ is the total system energy of atomic interaction, and $E_{ij}^{\mathrm{REBO}}$, $E_{ij}^{\mathrm{LJ}}$ describe the REBO potential and the LJ potential between atom $i$ and $j$, respectively. As part of the REBO term in the AIREBO potential, there are two cutoff distances in the switching function that controls the breaking of C–C bonds, which by default are 1.7 Å and 2.0 Å, respectively [41]. In this study, the smaller cutoff distance is modified to 1.92 Å to better capture the stress-strain relation of graphene benchmarked by DFT calculations, as has been used and validated by many previous studies [42–46]. The cutoff distance of the LJ term is set as 6.8 Å [29,47]. The integration time step is set as 1 fs. Periodic boundary conditions are applied to two in-plane dimensions and a fixed boundary condition is used in the perpendicular out-of-plane dimension. The in-plane dimensions of the

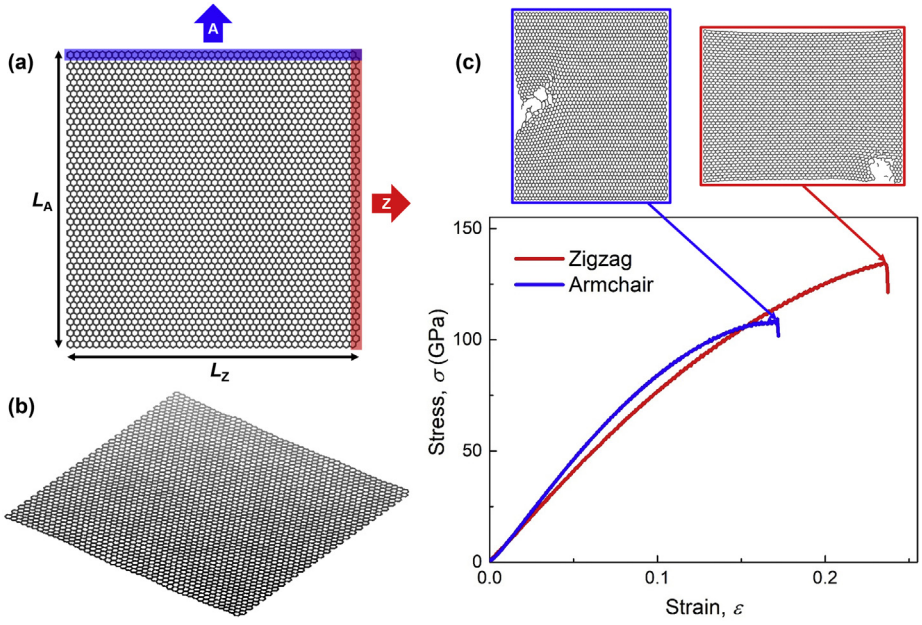


**Fig. 1.** Model setup and simulation results of pristine graphene. (a) Schematic of pristine graphene and illustration of tensile loading directions. (b) Morphology of monolayer graphene after running for equilibrium at 300 K. (c) Stress-strain curves and fracture modes of pristine graphene upon zigzag and armchair loadings. (A colour version of this figure can be viewed online).

simulation box (~175 Å × 175 Å) are set to be larger than the dimensions of graphene sheets (~110 Å × 110 Å) such that the distance from the edge of graphene sheets to the edge of the box is larger than the cutoff distance of AIREBO potential in which case the boundary effect is eliminated. In addition, the dimensions of simulation box will guarantee an enough space for the graphene sheet to be stretched until failure. After the generation of an ensemble of random velocity at 300 K, the system is running for equilibrium at 300 K in the isothermal-isobaric (NPT) ensemble with the Nose-Hoover thermostat [48] for 50 ps. The 3D morphology of graphene sheet after running for equilibrium in the NPT ensemble is shown in Fig. 1(b), where the maximum out-of-plane fluctuation of the rippling is ~ 2 Å. The loading scenario is simulated in the canonical (NVT) ensemble at the same temperature. Tensile loading is exerted based on the deformation-control method by assigning displacement at a constant speed to a 3 $\mathring{A}$ wide atom stripe at one end, while holding a 3 Å wide atom stripe at the other end immobile in all three dimensions. Strain rate applied in the MD simulation is $10^9$ $s^{-1}$[49]. The method to calculate the stress of a loaded graphene sheet is described as follows. The stress tensor $S_{ij}^{\alpha}$ for atom $\alpha$ is firstly calculated by the following formula, where $i$ and $j$ take on $x$, $y$ or $z$ to generate the 6 components of the symmetric tensor.

$$S_{ij}^{\alpha}=\frac{1}{2}m^{\alpha}v_i^{\alpha}v_j^{\alpha}+\sum_{\beta=1}^{n}r_{\alpha\beta}^{j}f_{\alpha\beta}^{i} \tag{2}$$

where $m^{\alpha}$ and $v^{\alpha}$ are the mass and velocity of atom $\alpha$; $r_{\alpha\beta}$ and $f_{\alpha\beta}$ are the distance and force between atoms $\alpha$ and $\beta$. After the calculation of stress tensor on each individual atom, the equivalent stress $\sigma$ of a graphene sheet is calculated based on von Mises stress

$$\sigma=\sqrt{\frac{1}{2}\left[\left(\sigma_{xx}-\sigma_{yy}\right)^2+\left(\sigma_{yy}-\sigma_{zz}\right)^2+\left(\sigma_{zz}-\sigma_{xx}\right)^2+6\left(\sigma_{xy}^2+\sigma_{yz}^2+\sigma_{zx}^2\right)\right]} \tag{3}$$

where$\sigma_{ij}=\frac{1}{V_0}\sum_{\gamma=1}^{n}S_{ij}^{\gamma}$where $V_0=L_Z L_A t$ is the initial volume, and $t=$ 3.4 Å is the equivalent thickness of monolayer graphene [52]. Fig. 1(c) shows the calculated stress-strain curves of pristine graphene under the two loading directions. The obtained curve shapes and failure stresses/strains in zigzag and armchair directions are in good agreement with previous studies [42,50,51,53], which validates the simulation setup. It is notable and important that both failure stress and strain in zigzag direction (referred to as zigzag/armchair failure stress/strain below) are higher than those in armchair direction, while Young's modulus is slightly lower within a small strain, revealing the intrinsic anisotropic mechanical property of pristine monolayer graphene. The fracture modes in Fig. 1(c) show that in both directions, fracture initiates on the unloaded edge. As is widely acknowledged, the mechanical behavior of materials can be altered and fine-tuned by introducing certain types of defects. Hence, it is rational to consider the possibility to fine-tune the anisotropy of graphene through rational design of defects. For example, can we use defect design to create an isotropic graphene sheet? Can we intensify the anisotropy of graphene? Can we design graphene that is stronger in one direction but more stretchable in the other?

## 3. Basic defect designs

To get started with the fine-tuning of anisotropic property using defect engineering, the influence of basic defect elements on the mechanical properties and the potential of tuning anisotropy are investigated. In this section, the influences of defect length, obliquity, offset from the center, and number of parallel defects are separately discussed. Defect width is fixed at two times of C–C bond length and is not a variable in this study.

### 3.1. Centered line defect with variable length

Single centered line defect in zigzag or armchair direction (referred to as zigzag or armchair defect below) is studied first. To illustrate how introducing a single centered line defect affects the mechanical properties of the graphene sheet, MD simulations are conducted to study graphene with single centered line defect with a length of half the graphene edge length, i.e., $L_D = 0.5L_Z$ for zigzag defect or $L_D = 0.5L_A$ for armchair defect, of which the results are presented in Fig. 2. Fig. 2(a) and (b) demonstrate the deformation and fracture modes of defected graphene by showing the morphologies of unloaded, deformed, and fractured graphene sheets. For the graphene sheet with zigzag defect shown in Fig. 2(a), upon zigzag loading, the line defect is lengthened and the fracture initiates from along the defect, different from the pristine scenario where fracture initiates on the graphene edge. Upon armchair loading, the line defect swells and the fracture initiates at the defect tip. A graphene sheet with an armchair defect exhibits similar deformation and fracture modes to its counterpart with zigzag defect, as is illustrated in Fig. 2(b). If the loading direction is perpendicular to the line defect, the defect swells and fracture initiates at the tip where it is the easiest for a rupture to occur, and ultimately leading to an early failure. Fig. 2(c) and (d) present the calculated stress-strain curves of defected graphene with the failure stress and strain of the pristine counterpart for comparison. When the loading and the defect are parallel, a minor degradation of mechanical behavior is shown compared to pristine graphene, while the loading and the defect are perpendicular, both failure stress and strain decrease significantly. It is notable that for graphene with armchair defect, the armchair direction becomes the stronger and more stretchable direction, flipping the anisotropy of graphene.

After looking into the above illustrative examples of centered line defect, a systematic parametric study is carried out to examine the influence of defect length, and the results are summarized in Fig. 3. Fig. 3(a) and (b) show the failure stress and strain of graphene with zigzag defect of various lengths. Results show that upon zigzag loading, both failure stress and strain exhibit minor, unpatterned change with increasing defect length, suggesting that the zigzag defect has a random but insignificant influence on the zigzag mechanical properties. Upon armchair loading, however, failure stress decreases monotonously as the defect length increases. Failure strain also shows a decreasing tendency, yet the rate of decrease slows down and the failure strain remains relatively unchanged when the defect length is above $0.3L_Z$. Fig. 3(c) and (d) present the parametric study result of graphene with armchair defect. Upon zigzag loading, as is perpendicular to the line defect, failure stress and strain decrease in a similar fashion to graphene with zigzag defect subject to armchair loading. Upon armchair loading, as is parallel to the line defect, the defect length has a relatively insignificant influence, similar to the scenario of zigzag defect upon zigzag loading but with a reduced randomness level. The discussion of the influence of defect length leads to the conclusion that defect length poses weakening effect to the mechanical properties of graphene sheet only when the line defect is perpendicular to the loading, and that the influence intensifies as defect length increases. Mechanical property is fairly unchanged when the line defect and the loading are parallel. It can be observed in Fig. 3(a) and (b) that mechanical properties in the zigzag direction show up-and-down trends, while there exhibit very little up-and-downs in

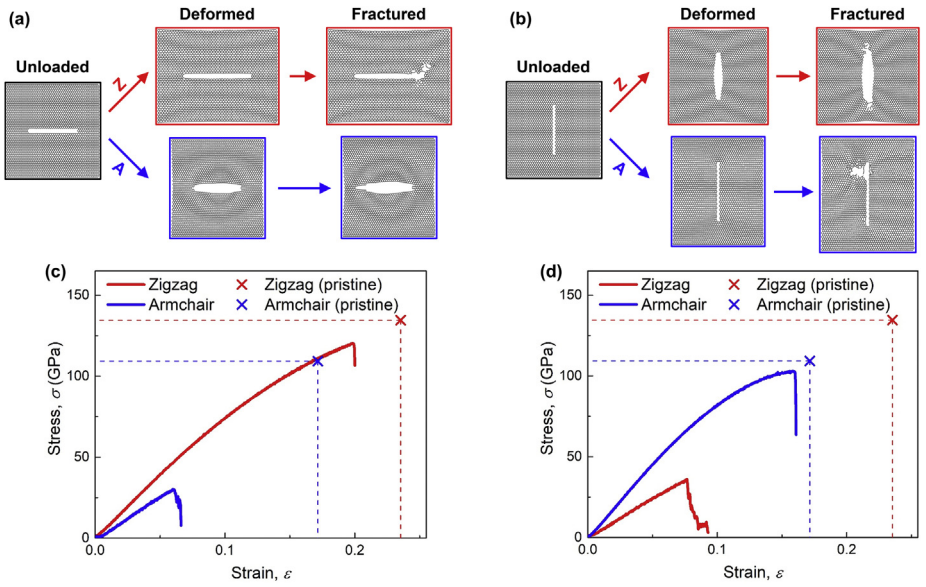


**Fig. 2.** Simulation results of graphene design with single centered line defect. Deformation and fracture modes of graphene sheets with (a) zigzag and (b) armchair defect. Stress-strain curves of graphene sheets with (c) zigzag and (d) armchair defect. The failure stresses and strains of the pristine monolayer graphene under two loading conditions are marked in the curve figures for comparison. (A colour version of this figure can be viewed online).

the armchair direction. Additionally, error bars (from running 4 sets of simulations for each data point) in the figures indicate that properties in the zigzag direction have relatively high data variation. The difference in data variation results from the fact that the influence of the defect length in the loading direction is too minor to cover the effect of other factors such as the unpredictable thermal effect; this further suggests that the absence of up-and-down trend in the armchair direction is due to the strong influence of a line defect in the perpendicular direction which covers all other competing factors. Concretely, if there is no up-and-down trend, the mechanical behavior of a defect pattern dominates over thermal fluctuations and vice versa. In the meantime, comparing results in Fig. 3(a, b) and Fig. 3(c, d), the mechanical properties in the zigzag direction has much more up-and-down trends and higher variation compared to those in the armchair direction regardless of the defect pattern, suggesting a higher level of intrinsic susceptibility to fluctuations in the zigzag direction. It is notable that a prominent dual relation between zigzag and armchair directions governs the design using centered line defect. Specifically, the scenario of zigzag defect upon armchair loading produces similar results as the scenario of armchair defect upon zigzag loading; the scenario of zigzag defect upon zigzag loading produces similar results as the scenario of armchair defect upon armchair loading.

To quantify the anisotropic property as well as to rationalize the defect design, the ratios between zigzag and armchair failure stresses $\sigma_{F,Z}/\sigma_{F,A}$, between zigzag and armchair failure strains $\varepsilon_{F,Z}/\varepsilon_{F,A}$, are calculated. The calculated results are then mapped onto a $\ln(\varepsilon_{F,Z}/\varepsilon_{F,A})$-versus-$\ln(\sigma_{F,Z}/\sigma_{F,A})$ graph (referred to as ratio graph below), transformed to 2D data points. The ratio graph, by definition, can be divided into the following four quadrants: Quadrant I ($\ln(\sigma_{F,Z}/\sigma_{F,A})>0$ and $\ln(\varepsilon_{F,Z}/\varepsilon_{F,A})>0$), where the failure stress and strain are both higher in zigzag direction than armchair direction; Quadrant II ($\ln(\sigma_{F,Z}/\sigma_{F,A})<0$ and $\ln(\varepsilon_{F,Z}/\varepsilon_{F,A})>0$), where the failure stress is higher in armchair direction, and the failure strain is higher in zigzag direction; Quadrant III ($\ln(\sigma_{F,Z}/\sigma_{F,A})<0$ and $\ln(\varepsilon_{F,Z}/\varepsilon_{F,A})<0$), where the failure stress and strain are both higher in armchair direction than zigzag direction; Quadrant IV ($\ln(\sigma_{F,Z}/\sigma_{F,A})>0$ and $\ln(\varepsilon_{F,Z}/\varepsilon_{F,A})<0$), where the failure stress is higher in zigzag direction, and the failure strain is higher in armchair direction. A defected graphene sheet is defined as "single-isotropic" if one of the values of $\ln(\sigma_{F,Z}/\sigma_{F,A})$ and $\ln(\varepsilon_{F,Z}/\varepsilon_{F,A})$ equals zero (data point landing on one of the axes of ratio graph), and is defined to be "double-isotropic" if both values equal zero (data point landing on the origin of ratio graph). The purpose of the 2D ratio graph is to visualize the anisotropy of defect designs with two properties being examined. By presenting the trace or distribution on the ratio graph when one or more parameters are changed, the technique schematizes how changing these parameters influences the anisotropic property of graphene sheet, which is not well understood in literature today. Fig. 3(e) shows the evolution on the ratio graph given an increasing defect length, arriving at the following conclusions:

1) Pristine graphene lies in Quadrant I on the ratio graph.
2) As the length of zigzag defect increases, the data point is driven away from the origin within Quadrant I, implicating an intensified anisotropy with respect to both failure stress and strain.
3) As the length of armchair defect increases, the data point is driven towards Quadrant III, implicating a reduced anisotropy with respect to both failure stress and strain at first, followed by the regain of anisotropy where armchair direction is the stronger direction in both failure stress and strain.
4) When driven toward Quadrant III, the data point passes the surrounding region of the origin, suggesting a potential strategy to design a nearly "double-isotropic" graphene.

### 3.2. Centered line defect with variable tilting angle

In this section, graphene with a centered oblique line defect is studied, featured by a defect tilting angle $\theta$ defined as the angle between the line defect and the zigzag direction. It is shown via MD simulation that an oblique line defect lowers the failure stresses and strains of graphene in both directions and the effect is equivalent to projecting the oblique line defect onto zigzag and armchair directions and acting as two orthogonal components. Simulation of a graphene design with a tilting angle of $\theta = 30^\circ$ and $\theta = 60^\circ$ are described in Fig. S1 in *Supplementary Information* as two examples

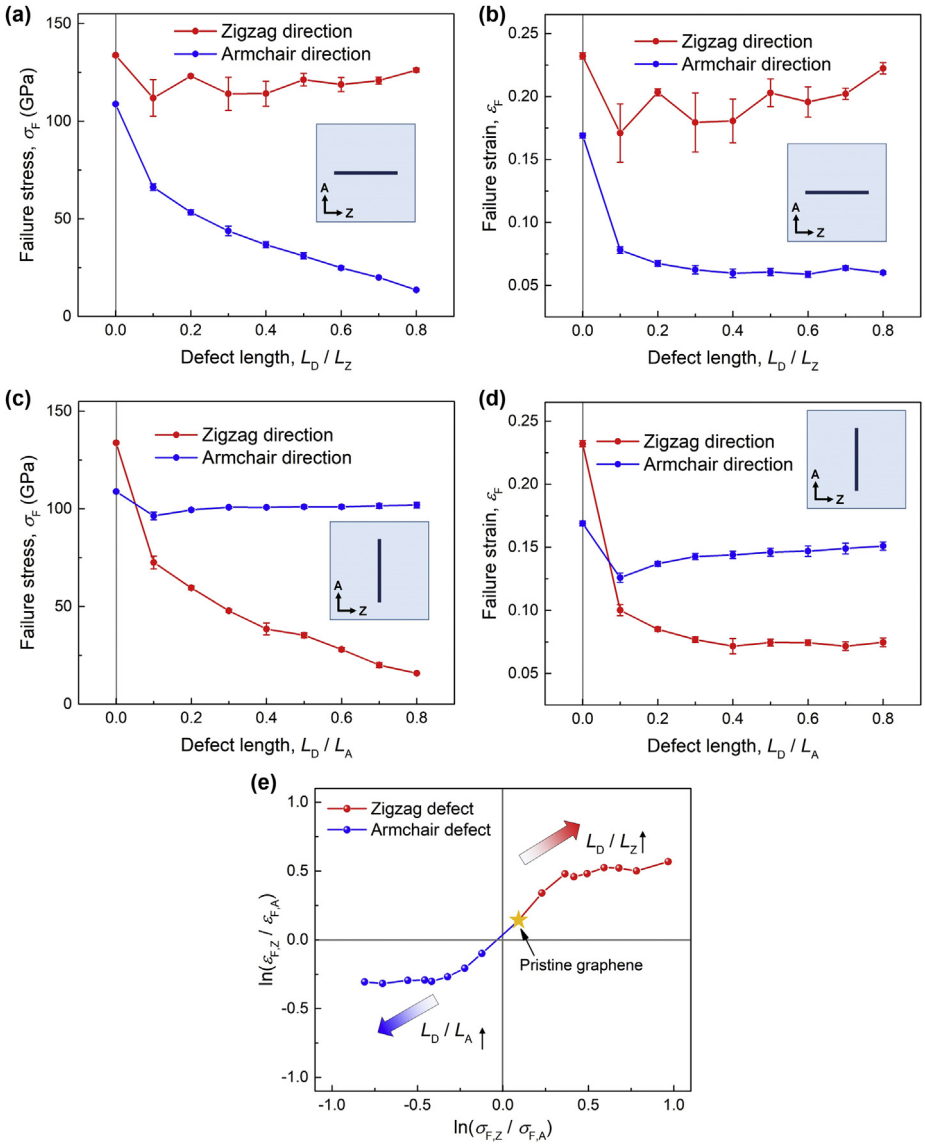


**Fig. 3.** Parametric study of graphene with single centered line defect with respect to defect length. Influence of defect length on (a) the failure stress and (b) failure strain of graphene with zigzag defect. Influence of defect length on (c) the failure stress and (d) failure strain of graphene with armchair defect. Zero defect length corresponds to pristine graphene. (e) Evolution of data points with increasing defect length on ratio graph. Data point corresponding to pristine graphene is marked with a star symbol. (A colour version of this figure can be viewed online).

to illustrate above anisotropic mechanical responses as well as the deformation and fracture modes. A more systematic parametric study of defect tilting angle $\theta$ is then carried out and summarized in Fig. S2. Fig. 4(a) shows the evolution of data points on the ratio graph given an increasing defect tilting angle $\theta$. As $\theta$ increases, the result is driven from Quadrant I towards Quadrant III, implicating a reduced anisotropy with respect to both failure stress and strain at first, followed by the regain of anisotropy where armchair direction is stronger in both failure stress and strain. The evolution of data points on the ratio graph demonstrates a similar path as the scenario of centered line defect with a variable length. This evolutionary pattern can be accounted for by the fact that the higher failure stress and strain are always in the same direction and the stronger direction is switchable. It is also noticeable that the evolutionary path on the ratio graph passes the surrounding region of the origin, implying that the defect design featured by oblique line defect is promising to produce a double-isotropic graphene sheet.

### 3.3. Line defect with an offset from the center

Single line defect in zigzag or armchair direction but with an offset from the center is studied as follows, where the element of asymmetry comes into play. It is of crucial importance to grasp an understanding how an offset defect affects the mechanical properties, because for complex patterned design involving multiple defects, most of the defects are actually offset with respect to the center of the graphene sheet. For the discussion in this section, the offset is introduced in the armchair direction for zigzag defect, and is in the zigzag direction for armchair defect. Examples of the simulation are provided in Fig. S3, showing that the offsetting of line defect in fact has a rather insignificant effect on the mechanical properties and fracture modes of defected graphene. In spite of not being influential according to the simulation results, the influence of offset distance $e_D$ on the mechanical properties and the potential of tuning anisotropy of graphene is examined, of which the results are summarized in Fig. S4. Results of parametric study are

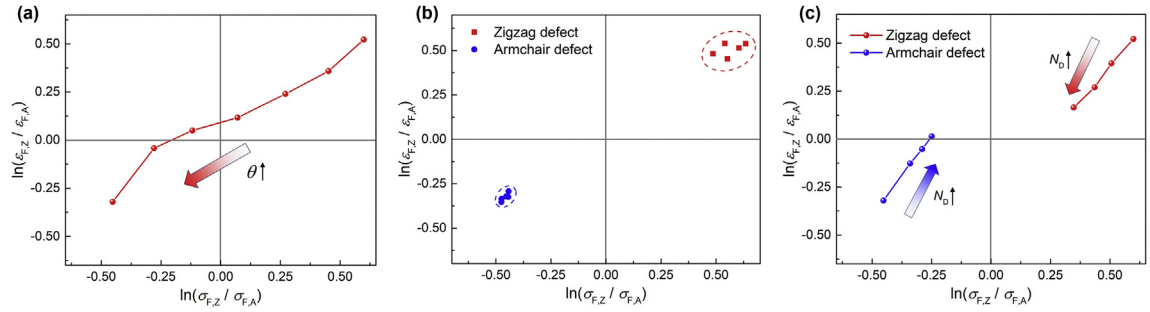


**Fig. 4.** Evolutionary paths or distribution of data points on the ratio graph. (a) Evolutionary path of data points of graphene with centered oblique line defect when the tilting angle $\theta$ increases. (b) Distribution of data points of graphene with offset line defect with various offset distances $e_D$. (c) Evolutionary path of data points of graphene with multiple parallel line defects with increasing defect number $N_D$.(A colour version of this figure can be viewed online).

converted to a representation on the ratio graph as Fig. 4(b). As is shown, no clear evolutionary path is detected as the offset distance increases, and scenarios of zigzag and armchair defect with various offset distances are clustered within a relatively small region in Quadrant I and Quadrant III. Therefore, introducing an offset to a single line defect may not effectively change the anisotropic property of the graphene sheet and its influence on mechanical properties is rather limited. Notably, the zigzag defect has a larger clustering area on the ratio graph, indicating a higher level of intrinsic susceptibility to uncertainty in the zigzag direction, as has been suggested in Fig. 3.

### 3.4. Parallel uniform line defects

Patterned defect designs usually involve multiple defects. Amongst the most straightforward designs with multiple line defects are parallel uniform line defects. To pursue a further simplicity and to reduce the design space, in this study, the following simplifications are adopted: 1) Parallel defects are only in zigzag or armchair direction. 2) All defects have the same and fixed length. 3) Graphene sheets are equally sectioned by parallel defects. Above simplifications make it possible that the number of defects is the only design variable. To study how the inclusion of multiple parallel uniform defects and their potential interplay affects the mechanical properties of graphene, MD simulations of graphene with parallel uniform line defects with a defect number $N_D = 3$ are performed. Results show that the failure strain can be enhanced compared to graphene with a single defect in the direction perpendicular to the parallel defect, thus heading towards Quadrant II on the ratio graph, as is detailed in Fig. S5. After discovering the new tuning possibility of design with multiple parallel defects, the influence of defect number $N_D$ on the mechanical properties is discussed, showing the capability to stably enhance the failure strain with increasing $N_D$, as is detailed and summarized in Fig. S6. The parametric results are then mapped onto the ratio graph to provide insights to anisotropy-oriented defect design, as is illustrated in Fig. 4(c). It is shown that as the defect number increases, the parallel zigzag defect design is driven from Quadrant I down towards Quadrant IV but does not end up entering, while the parallel armchair defect design immigrates from Quadrant III to Quadrant II. It is therefore concluded that the design of parallel uniform line defects advances the tuning capability of graphene anisotropy by exploiting a new region on the ratio graph which is inaccessible for designs using single line defects.

## 4. Complex patterned defect design

Although the above defect designs with basic elements have exhibited the capability to fine-tune the mechanical anisotropy of the graphene sheet, a few limitations exist. Firstly, designs with a single defect has yet to be able to produce data points in Quadrant IV or deep into Quadrant II, Secondly, the fine-tuning of anisotropy using a single defect has a sacrificial nature, namely, at least one of failure stress and strain are weakened compared to pristine graphene sheet during the tuning, and no improvement in mechanical property can be obtained. In this section, two specific complex patterned defect designs are proposed, namely, network-like graphene kirigami and graphene kirigami with parallel interior and exterior cuts, which may be contributive to new unexplored anisotropic properties and help overcome the limitations of designs with basic defects. Fig. 5 shows the critical geometric parameters of these designs. The design of network-like graphene kirigami is schematized in Fig. 5(a), where the set of parameters addresses the lengths of various cuts as well as the positions relative to the graphene edge. The purpose of the network-like graphene kirigami is to achieve the entry into Quadrant IV which is not yet accessible for designs discussed above. Landing in Quadrant IV requires a higher zigzag failure stress together with a higher armchair failure strain. The zigzag-oriented central cut is designed to maintain the zigzag strength and improve the armchair stretchability. The designs of graphene kirigami with parallel interior and exterior cuts are illustrated in Fig. 5(b) and (c), corresponding to designs consisting of zigzag and armchair defects, respectively. The purpose of this design is to produce graphene of which the stretchability outperforms that of the pristine graphene utilizing the combination of interior and exterior cuts [47]. Specifically, parallel zigzag defects are aimed to improve the stretchability in the armchair direction, and parallel armchair defects are aimed to improve the stretchability in the zigzag direction. To reduce the design space, graphene sheet is tri-sectioned by line defects by default, leading to only two independent parameters being in the system, i.e. the length of the central interior defect $L_1$ and the length of the exterior defect $L_2$. To experimentally realize the complex designs proposed in this study, patterned graphene sheets can be fabricated by a variety of methods such as etching techniques using thermally activated metallic nanoparticles [54,55], atomic force microscopy anodic oxidation [56], and scanning tunneling microscopy lithography [57], which can produce ultrafine patterns on monolayer and multilayer graphene.

As an example, the design of network-like graphene kirigami with the following geometric parameters is simulated: $(L_{Z1}, L_{Z2}, L_{A1}, L_{A2}, D_{Z1}, D_{Z2}, D_{A1}, D_{A2}) = (0.5L_Z, 0.2L_Z, 0.3L_A, 0.2L_A, 0.15L_Z, 0.1L_Z, 0.2L_A, 0.1L_A)$, of which the deformation and fracture modes and stress-strain relation are detailed in Fig. S7. Due to the high complexity of the design, the design space becomes too vast to be practical to study the influences of all design parameters and their

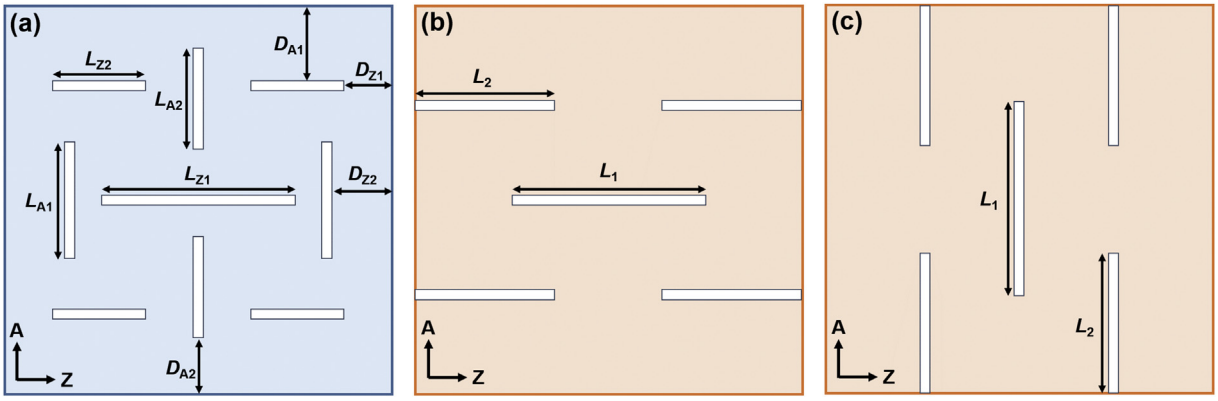


**Fig. 5.** Complex defect pattern designs. (a) Network-like graphene kirigami, (b) graphene kirigami with parallel zigzag interior and exterior cuts, and (c) graphene kirigami with parallel armchair interior and exterior cuts. (A colour version of this figure can be viewed online).

interplay exhaustively. Fig. 6(a) shows the distribution on the ratio graph of a couple of designs of network-like graphene kirigami. It is observed that a majority of data points successfully land in Quadrant IV and some data points are also distributed in Quadrant I.

Despite the fact that the design of network-like graphene kirigami has made its way to Quadrant IV, the data points are in fact relatively close to the origin on the ratio graph, indicating a weak mechanical anisotropy. Additionally, the realization is sacrificial, entering Quadrant IV by lowering zigzag failure strain. At this stage, the design of graphene kirigami with parallel interior and exterior cuts is anticipated, which has more potential to drive deeper into Quadrant IV by pursuing stretchability superior to the pristine monolayer graphene. To illustrate, MD simulations of graphene kirigami with zigzag parallel interior and exterior cuts with the parameters $(L_1, L_2) = (0.6L_Z, 0.35L_Z)$ are conducted. Results indicate a non-sacrificial nature of the present design to tuning of mechanical anisotropy, as are provided in detail in Fig. S8. A systematic parametric study with respect to the parameter pair $(L_1, L_2)$ is also provided in Fig. S9, showing that the failure stress increases with decreasing lengths of both interior and exterior cuts, while the failure strain increases with increasing lengths of both interior and exterior cuts. Combinations of high $L_1$ and $L_2$ can produce higher failure strain than pristine graphene, making the design strategy non-sacrificial.

Given the 2D parametric study results, the insight into the design of graphene kirigami with parallel interior and exterior cuts contribute to new anisotropy tuning capability can be readily discussed, by mapping parametric study results onto the ratio graph as follows. According to Fig. S9(c-f), the most drastic failure strain change happens where the central interior cut is relatively long, data points corresponding to $L_1/L_Z$ and $L_1/L_A \in [0.55, 0.60, 0.65]$ are therefore selected to provide more prominent evolutionary paths on the ratio graph. $L_2/L_Z$ and $L_2/L_A$ still use the full results of parametric study, increasing from 0.05 to 0.40, to illustrate the longest path as has been studied. The evolution of the current graphene kirigami design on ratio graph is summarized in Fig. 6(b), with the data point region obtained by network-like graphene kirigami design as a comparison. Results show that for design of the zigzag interior and exterior defects, data points migrate down from Quadrant I to Quadrant IV as the length of exterior defects increases, while for the armchair counterparts, data points migrate up from Quadrant III deep into Quadrant II. In addition, compared to network-like design, the design with parallel interior and exterior defects not only can dive much deeper into Quadrant II and Quadrant IV but also has a significantly vaster attainable region across the 2D plane. An interesting future direction to this work involves using methods like machine learning to optimize for desired material properties [58–61] and to expand defect designs into the third dimension by adding curvature.

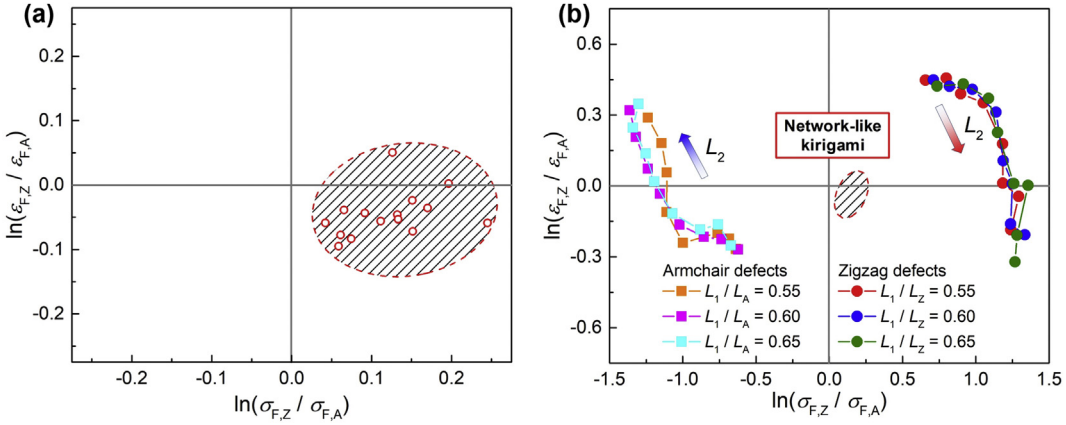


**Fig. 6.** Distribution or evolutionary paths of data points of complex patterned defect designs on 2D ratio graph. (a) Distribution of data points of a variety of designs of network-like graphene kirigami. (b) Evolution of data points of graphene kirigami with parallel interior and exterior cuts. The attainable region of network-like graphene kirigami design is marked on the graph to draw comparison. (A colour version of this figure can be viewed online).

## 5. Concluding remarks

In this paper, a defect engineering strategy is adopted to tune the anisotropic property of monolayer graphene. Mechanical properties of various defect designs, from simple single-line defect designs to more complex designs with multiple defects, are systematically studied using MD simulation. For designs consisting of basic defect elements, the influences of defect length, obliquity, and offset from the center, number of parallel defects are separately discussed. For more complex defect designs, network-like graphene kirigami and graphene kirigami with parallel interior and exterior cuts are investigated. A novel ratio graph is proposed to visualize and rationalize the tuning of mechanical anisotropy of defected graphene sheet, which has ultimately helped answer the questions like how to make an isotropic graphene sheet, how to intensify the anisotropy of graphene, and design a defected graphene which is stronger in one direction and more stretchable in the other. Through our defect designs, all the four quadrants of the 2D ratio graph are covered, indicating a high capability and versatility of fine-tuning the mechanical properties of graphene in both directions. This research investigates the tunability of graphene mechanical anisotropy via defect design, which may shed light on the new possibility of fine-tuning mechanical properties of other 2D materials as well as the performance improvement of state-of-the-art applications with graphene usage such as stretchable electronics, supercapacitor devices, among others. More complex design such as designs involving curved defects as well as other 2D materials will be covered in future work.

## Acknowledgements

The authors acknowledge support from the Extreme Science and Engineering Discovery Environment (XSEDE) at the Pittsburgh Supercomputing Center (PSC) through allocation TG-DMR180085, by National Science Foundation grant number ACI-1548562. Additionally, the authors acknowledge support from an NVIDIA GPU Seed Grant and the Savio computational cluster resource provided by the Berkeley Research Computing program.

## Appendix A. Supplementary data

Supplementary data to this article can be found online at https://doi.org/10.1016/j.carbon.2019.09.008.

## References

[1] C. Berger, Z. Song, T. Li, X. Li, A.Y. Ogbazghi, R. Feng, Z. Dai, A.N. Marchenkov, E.H. Conrad, P.N. First, W.A. de Heer, Ultrathin epitaxial Graphite: 2D electron gas properties and a route toward graphene-based nanoelectronics, J. Phys. Chem. B 108 (52) (2004) 19912–19916.
[2] F. Withers, M. Dubois, A.K. Savchenko, Electron properties of fluorinated single-layer graphene transistors, Phys. Rev. B 82 (7) (2010) 073403.
[3] B. Liu, K. Zhou, Recent progress on graphene-analogous 2D nanomaterials: properties, modeling and applications, Prog. Mater. Sci. 100 (2019) 99–169.
[4] A.A. Balandin, S. Ghosh, W. Bao, I. Calizo, D. Teweldebrhan, F. Miao, C.N. Lau, Superior thermal conductivity of single-layer graphene, Nano Lett. 8 (3) (2008) 902–907.
[5] A.A. Balandin, Thermal properties of graphene and nanostructured carbon materials, Nat. Mater. 10 (2011) 569.
[6] C. Lee, X. Wei, J.W. Kysar, J. Hone, Measurement of the elastic properties and intrinsic strength of monolayer graphene, Science 321 (5887) (2008) 385–388.
[7] P. Zhang, L. Ma, F. Fan, Z. Zeng, C. Peng, P.E. Loya, Z. Liu, Y. Gong, J. Zhang, X. Zhang, P.M. Ajayan, T. Zhu, J. Lou, Fracture toughness of graphene, Nat. Commun. 5 (2014) 3782.
[8] K.S. Novoselov, A.K. Geim, S.V. Morozov, D. Jiang, Y. Zhang, S.V. Dubonos, I.V. Grigorieva, A.A. Firsov, Electric field effect in atomically thin carbon films, Science 306 (5696) (2004) 666–669.
[9] Z. Xu, C. Gao, Graphene fiber: a new trend in carbon fibers, Mater. Today 18 (9) (2015) 480–492.
[10] Z. Xu, H. Sun, X. Zhao, C. Gao, Ultrastrong fibers assembled from giant graphene oxide sheets, Adv. Mater. 25 (2) (2013) 188–193.
[11] D. Cohen-Tanugi, J.C. Grossman, Mechanical strength of nanoporous graphene as a desalination membrane, Nano Lett. 14 (11) (2014) 6171–6178.
[12] S.P. Koenig, N.G. Boddeti, M.L. Dunn, J.S. Bunch, Ultrastrong adhesion of graphene membranes, Nat. Nanotechnol. 6 (2011) 543.
[13] K.S. Kim, Y. Zhao, H. Jang, S.Y. Lee, J.M. Kim, K.S. Kim, J.-H. Ahn, P. Kim, J.-Y. Choi, B.H. Hong, Large-scale pattern growth of graphene films for stretchable transparent electrodes, Nature 457 (2009) 706.
[14] H. Jang, Y.J. Park, X. Chen, T. Das, M.-S. Kim, J.-H. Ahn, Graphene-based flexible and stretchable electronics, Adv. Mater. 28 (22) (2016) 4184–4202.
[15] C. Martin-Olmos, H.I. Rasool, B.H. Weiller, J.K. Gimzewski, Graphene MEMS: AFM probe performance improvement, ACS Nano 7 (5) (2013) 4164–4170.
[16] J.S. Bunch, A.M. van der Zande, S.S. Verbridge, I.W. Frank, D.M. Tanenbaum, J.M. Parpia, H.G. Craighead, P.L. McEuen, Electromechanical resonators from graphene sheets, Science 315 (5811) (2007) 490–493.
[17] A. Reserbat-Plantey, K.G. Schädler, L. Gaudreau, G. Navickaite, J. Güttinger, D. Chang, C. Toninelli, A. Bachtold, F.H.L. Koppens, Electromechanical control of nitrogen-vacancy defect emission using graphene NEMS, Nat. Commun. 7 (2016) 10218.
[18] J. Zhu, A.S. Childress, M. Karakaya, S. Dandeliya, A. Srivastava, Y. Lin, A.M. Rao, R. Podila, Defect-engineered graphene for high-energy- and high-power-density supercapacitor devices, Adv. Mater. 28 (33) (2016) 7185–7192.
[19] Y. Zhu, S. Murali, M.D. Stoller, K.J. Ganesh, W. Cai, P.J. Ferreira, A. Pirkle, R.M. Wallace, K.A. Cychosz, M. Thommes, D. Su, E.A. Stach, R.S. Ruoff, Carbon-based supercapacitors produced by activation of graphene, Science 332 (6037) (2011) 1537–1541.
[20] Y. Wang, Z. Shi, Y. Huang, Y. Ma, C. Wang, M. Chen, Y. Chen, Supercapacitor devices based on graphene materials, J. Phys. Chem. C 113 (30) (2009) 13103–13107.
[21] T.O. Wehling, K.S. Novoselov, S.V. Morozov, E.E. Vdovin, M.I. Katsnelson, A.K. Geim, A.I. Lichtenstein, Molecular doping of graphene, Nano Lett. 8 (1) (2008) 173–177.
[22] D. Soriano, D.V. Tuan, S.M.M. Dubois, M. Gmitra, A.W. Cummings, D. Kochan, F. Ortmann, J.-C. Charlier, J. Fabian, S. Roche, Spin transport in hydrogenated graphene, 2D Mater. 2 (2) (2015) 022002.
[23] S.-K. Chien, Y.-T. Yang, C.o.-K. Chen, Influence of chemisorption on the thermal conductivity of graphene nanoribbons, Carbon 50 (2) (2012) 421–428.
[24] Z. Ni, H. Bu, M. Zou, H. Yi, K. Bi, Y. Chen, Anisotropic mechanical properties of graphene sheets from molecular dynamics, Physica B 405 (5) (2010) 1301–1306.
[25] B.B. Fan, X.B. Yang, R. Zhang, Anisotropic mechanical properties and Stone–Wales defects in graphene monolayer: a theoretical study, Phys. Lett. A 374 (27) (2010) 2781–2784.
[26] L.F.C. Pereira, B. Mortazavi, M. Makaremi, T. Rabczuk, Anisotropic thermal conductivity and mechanical properties of phagraphene: a molecular dynamics study, RSC Adv. 6 (63) (2016) 57773–57779.
[27] L. Han, L. Wang, J. Song, M.C. Boyce, C. Ortiz, Direct quantification of the mechanical anisotropy and fracture of an individual exoskeleton layer via uniaxial compression of micropillars, Nano Lett. 11 (9) (2011) 3868–3874.
[28] M.K. Blees, A.W. Barnard, P.A. Rose, S.P. Roberts, K.L. McGill, P.Y. Huang, A.R. Ruyack, J.W. Kevek, B. Kobrin, D.A. Muller, P.L. McEuen, Graphene kirigami, Nature 524 (2015) 204.
[29] T.C. Shyu, P.F. Damasceno, P.M. Dodd, A. Lamoureux, L. Xu, M. Shlian, M. Shtein, S.C. Glotzer, N.A. Kotov, A kirigami approach to engineering elasticity in nanocomposites through patterned defects, Nat. Mater. 14 (2015) 785.
[30] N. Wei, Y. Chen, K. Cai, J. Zhao, H.-Q. Wang, J.-C. Zheng, Thermal conductivity of graphene kirigami: ultralow and strain robustness, Carbon 104 (2016) 203–213.
[31] D.G. Papageorgiou, I.A. Kinloch, R.J. Young, Mechanical properties of graphene and graphene-based nanocomposites, Prog. Mater. Sci. 90 (2017) 75–127.
[32] C.-T. Chen, F.J. Martin-Martinez, S. Ling, Z. Qin, M.J. Buehler, Nacre-inspired design of graphene oxide–polydopamine nanocomposites for enhanced mechanical properties and multi-functionalities, Nano Futures 1 (1) (2017) 011003.
[33] C.T. Chen, G.X. Gu, Effect of constituent materials on composite performance: exploring design strategies via machine learning, Adv. Theor. Simulat. 2 (6) (2019), 1900056.
[34] J. Bai, X. Zhong, S. Jiang, Y. Huang, X. Duan, Graphene nanomesh, Nat. Nanotechnol. 5 (2010) 190.
[35] L. Jiang, Z. Fan, Design of advanced porous graphene materials: from graphene nanomesh to 3D architectures, Nanoscale 6 (4) (2014) 1922–1945.
[36] S. Zhu, Y. Huang, T. Li, Extremely compliant and highly stretchable patterned graphene, Appl. Phys. Lett. 104 (17) (2014) 173103.
[37] L. Qiu, D. Li, H.-M. Cheng, Structural control of graphene-based materials for unprecedented performance, ACS Nano 12 (6) (2018) 5085–5092.
[38] S. Plimpton, Fast parallel algorithms for short-range molecular dynamics, J. Comput. Phys. 117 (1) (1995) 1–19.
[39] H. Zhao, N.R. Aluru, Temperature and strain-rate dependent fracture strength of graphene, J. Appl. Phys. 108 (6) (2010) 064321.
[40] Z. Qi, F. Zhao, X. Zhou, Z. Sun, H.S. Park, H. Wu, A molecular simulation analysis of producing monatomic carbon chains by stretching ultranarrow graphene nanoribbons, Nanotechnol 21 (26) (2010) 265702.
[41] S.J. Stuart, A.B. Tutein, J.A. Harrison, A reactive potential for hydrocarbons with

intermolecular interactions, J. Chem. Phys. 112 (14) (2000) 6472–6486.
[42] Y. Wei, J. Wu, H. Yin, X. Shi, R. Yang, M. Dresselhaus, The nature of strength enhancement and weakening by pentagon–heptagon defects in graphene, Nat. Mater. 11 (2012) 759.
[43] R. Grantab, V.B. Shenoy, R.S. Ruoff, Anomalous strength characteristics of tilt grain boundaries in graphene, Science 330 (6006) (2010) 946–948.
[44] C. Wang, Y. Liu, L. Lan, H. Tan, Graphene wrinkling: formation, evolution and collapse, Nanoscale 5 (10) (2013) 4454–4461.
[45] J. Wu, Y. Wei, Grain misorientation and grain-boundary rotation dependent mechanical properties in polycrystalline graphene, J. Mech. Phys. Solids 61 (6) (2013) 1421–1432.
[46] T. Zhang, X. Li, S. Kadkhodaei, H. Gao, Flaw insensitive fracture in nanocrystalline graphene, Nano Lett. 12 (9) (2012) 4605–4610.
[47] Z. Qi, D.K. Campbell, H.S. Park, Atomistic simulations of tension-induced large deformation and stretchability in graphene kirigami, Phys. Rev. B 90 (24) (2014) 245437.
[48] W.G. Hoover, Canonical dynamics: equilibrium phase-space distributions, Phys. Rev. A 31 (3) (1985) 1695–1697.
[49] H. Zhao, K. Min, N.R. Aluru, Size and chirality dependent elastic properties of graphene nanoribbons under uniaxial tension, Nano Lett. 9 (8) (2009) 3012–3015.
[50] Y.Y. Zhang, Y.T. Gu, Mechanical properties of graphene: effects of layer number, temperature and isotope, Comput. Mater. Sci. 71 (2013) 197–200.
[51] Y. Chu, T. Ragab, C. Basaran, The size effect in mechanical properties of finite-sized graphene nanoribbon, Comput. Mater. Sci. 81 (2014) 269–274.
[52] Y. Huang, J. Wu, K.C. Hwang, Thickness of graphene and single-wall carbon nanotubes, Phys. Rev. B 74 (24) (2006) 245413.
[53] Q.-X. Pei, Y.-W. Zhang, V.B. Shenoy, Mechanical properties of methyl functionalized graphene: a molecular dynamics study, Nanotechnol 21 (11) (2010) 115709.
[54] L.C. Campos, V.R. Manfrinato, J.D. Sanchez-Yamagishi, J. Kong, P. Jarillo-Herrero, Anisotropic etching and nanoribbon formation in single-layer graphene, Nano Lett. 9 (7) (2009) 2600–2604.
[55] S.S. Datta, D.R. Strachan, S.M. Khamis, A.T.C. Johnson, Crystallographic etching of few-layer graphene, Nano Lett. 8 (7) (2008) 1912–1915.
[56] S. Masubuchi, M. Ono, K. Yoshida, K. Hirakawa, T. Machida, Fabrication of graphene nanoribbon by local anodic oxidation lithography using atomic force microscope, Appl. Phys. Lett. 94 (8) (2009) 082107.
[57] L. Tapasztó, G. Dobrik, P. Lambin, L.P. Biró, Tailoring the atomic structure of graphene nanoribbons by scanning tunnelling microscope lithography, Nat. Nanotechnol. 3 (2008) 397.
[58] G.X. Gu, C.-T. Chen, D.J. Richmond, M.J. Buehler, Bioinspired hierarchical composite design using machine learning: simulation, additive manufacturing, and experiment, Mater. Horiz. 5 (5) (2018) 939–945.
[59] P.Z. Hanakata, E.D. Cubuk, D.K. Campbell, H.S. Park, Accelerated search and design of stretchable graphene kirigami using machine learning, Phys. Rev. Lett. 121 (25) (2018) 255304.
[60] C. Yang, Y. Kim, S. Ryu, G.X. Gu, Using convolutional neural networks to predict composite properties beyond the elastic limit, MRS Commun. (2019) 1–9.
[61] G. Pilania, C. Wang, X. Jiang, S. Rajasekaran, R. Ramprasad, Accelerating materials property predictions using machine learning, Sci. Rep. 3 (2013).